World Scientific
www.worldscientific.com

Multimodal nonlinear microscopy:
A powerful label-free method for supporting
standard diagnostics on biological tissues

Riccardo Cicchi*,†,¶ and Francesco Saverio Pavone*,†,‡,§

*National Institute of Optics
National Research Council (INO-CNR)
Largo E. Fermi 6, 50125 Florence, Italy

†European Laboratory for Nonlinear Spectroscopy (LENS)
University of Florence, Sesto Fiorentino, Italy

‡Department of Physics
University of Florence, Sesto Fiorentino, Italy

§International Center of Computational Neurophotonics (ICON)
Florence, Italy
¶riccardo.cicchi@ino.it

The large use of nonlinear laser scanning microscopy in the past decade paved the way for potential clinical application of this imaging technique. Modern nonlinear microscopy techniques offer promising label-free solutions to improve diagnostic performances on tissues. In particular, the combination of multiple nonlinear imaging techniques in the same microscope allows integrating morphological with functional information in a morpho-functional scheme. Such approach provides a high-resolution label-free alternative to both histological and immunohistochemical examination of tissues and is becoming increasingly popular among the clinical community. Nevertheless, several technical improvements, including automatic scanning and image analysis, are required before the technique represents a standard diagnostic method. In this review paper, we highlight the capabilities of multimodal nonlinear microscopy for tissue imaging, by providing various examples on colon, arterial and skin tissues. The comparison between images acquired using multimodal nonlinear microscopy and histology shows a good agreement between the two methods. The results demonstrate that multimodal nonlinear microscopy is a powerful label-free alternative to standard histopathological methods and has the potential to find a stable place in the clinical setting in the near future.

Keywords: Non-linear microscopy; tissue imaging.

1. Introduction

The histological examination currently represents the "gold standard" for tissue diagnostics. The method includes tissue cryo-sectioning, processing and labeling before the observation through white light wide-field microscopy. The largely used hematoxylin-eosin (H&E) staining allows highlighting only morphological features that are relevant for the diagnosis. A more detailed functional-chemical analysis of tissues under examination requires targeting molecules of interest by means of specific labels and observing using fluorescence microscopy in an immunohistochemical approach. Independent from the method used, a long protocol including dehydration, fixation, inclusion, labeling and observation is required to prepare tissue samples. In this depiction, an imaging technique able to provide similar information in a fast, reliable and label-free way would be suitable for improving diagnostic performances.

Nonlinear optical (NLO) microscopy allows label-free micron-scale resolution in highly scattering media such as biological tissues and is able to provide not only morphological but also functional information on the observed sample. NLO microscopy offers several advantages for tissue imaging with respect to other equivalent single-photon laser scanning imaging techniques such as confocal microscopy. First, the nonlinearity of the interaction allows selectively exciting only molecules located within an extremely confined volume around the focal point, hence improving spatial resolution. Second, the axial confinement of the excitation volume intrinsically provides optical sectioning capability, reducing photodamage and photo-toxic effects. Third, NLO microscopy employs NIR laser wavelengths that offer deep label-free imaging in biological tissues.[1,2] Further, scattered photons do not contribute to the excitation resulting in a spatial resolution that remains almost unchanged when imaging deep into an optically dense specimen.[3] NLO microscopy includes several laser scanning imaging techniques characterized by an interaction between light and the biological specimen mediated by two or more photons. Depending on the peculiar features, each technique is able to provide morphological and/or chemical information on the tissue under investigation. A particularly powerful approach for tissue classification consists in combining the techniques providing only morphological information with those providing functional information. In fact, this combination offers the potential to address the relationship between morphological features such as architecture, shape, symmetry and functional features. In a biological tissue, the relationship between morphology and function has to be strict, even if complex. Understanding this relationship can help in classifying tissue and open new insights for the comprehension of the pathological development.

Among NLO microscopy techniques able to provide morphological information, two-photon excited fluorescence (TPF) microscopy is the most popular and widespread technique. In TPF, an electronic molecular transition is excited by simultaneous absorption of two photons, each of them having one-half of the transition energy.[4] The technique was firstly implemented in a laser scanning microscope in 1990 by Denk *et al.*[5] The strong potential of this microscopic technique was demonstrated in the last 20 years by the growing number of studies in both biological and biomedical fields employing TPF microscopy[1,6,7] for tissue imaging.[8–12] TPF microscopy is able to provide label-free morphological information with sub-cellular resolution in both epithelium and connective tissue by exciting endogenous fluorescent molecules such as NADH, FAD and elastic fiber.[13,14] Recent studies demonstrated also its potential for *in vivo* imaging on skin of living subjects[15–18] and on brain of small animals.[19,20] Regarding clinical applications, now TPF skin imaging is becoming popular among the dermatological community.[21–23] Another NLO imaging technique, extremely powerful for label-free imaging of connective tissue, is second-harmonic generation (SHG) microscopy.[24–26] SHG microscopy is a coherent NLO imaging technique able to provide label-free, background-free, high-resolution images of biological molecules with large hyperpolarizability,[27,28] such as collagen,[29–31] muscle,[32–37] or microtubules.[38] SHG consists of a second-order scattering process occurring in specimens having a large hyperpolarizability and a structural anisotropy at the focal volume scale. These conditions are satisfied in collagen, muscle or microtubules, making SHG microscopy the perfect optical tool for imaging and investigating both molecular and supramolecular organization of these biological systems.[37,39] The studies conducted using SHG microscopy on cells,[40–42] cellular membranes,[43–47]

brain[38] and biological tissues[14,48,49] demonstrate the broad applicability of the technique. SHG is particularly powerful in providing background-free imaging of collagen[39,50] in various tissues such as cornea,[51,52] tendon,[53,54] and arteries.[55] SHG microscopy has already been used for investigating structural organization of collagen in human dermis,[56–60] keloid,[61–63] fibrosis,[64–66] thermally treated samples,[67–71] and also in tumor microenvironment.[72–78] SHG microscopy can be used to detect altered physiological conditions in various tissues, including muscle,[79,80] bones[81,82] and cartilages.[83,84] Combined TPF-SHG microscopy provides a powerful tool for imaging both epithelium and connective tissue. In fact, TPF microscopy offers high-resolution imaging of NADH in living cells and of elastin within connective tissue, while SHG enables the direct imaging of collagen. Combined TPF-SHG microscopy was successfully employed for studying physiological and pathological conditions of connective tissues, especially for cutaneous photoaging[22,85–87] and skin tumors.[59,67,88] Combining TPF and SHG microscopy is a powerful solution for label-free tissue imaging, however they are not able to provide functional information unless used in combination with other imaging techniques.

Vibrational microscopy techniques can provide label-free imaging of tissues in a morpho-chemical approach, enabling functional-chemical characterization of tissues by resolving the vibrational structure of the molecules contained in the sample itself. In fact, the vibrational spectrum of every biological specimen represents a specific fingerprint of its molecular components.[89] Spontaneous Raman scattering microscopy is the most popular vibrational microscopy technique. It provides label-free chemical information with the advantage of high resolution because it employs visible-NIR wavelengths for investigating transitions located in the IR range. However, due to the low crosssection of molecules within tissues, spontaneous Raman scattering microscopy is limited in terms of both sensitivity and imaging speed. Further, it does not provide the advantages of NLO microscopy. A significant step forward consists of coherent anti-Stokes Raman scattering (CARS) microscopy.[90] CARS microscopy is a nonlinear variant of spontaneous Raman scattering that uses two synchronized pulsed laser sources (pump and Stokes), with their frequency difference matching the vibrational transition to be investigated, for exciting a molecular transition. The interaction with a third pulse (probe) generates a detectable anti-Stokes signal. CARS microscopy allows investigating various molecular vibrations upon proper tuning of pump and Stokes beams. CARS microscopy also offers functional-chemical characterization of tissues by providing vibrational spectroscopic information at the scale of optical resolution,[91–93] with increased sensitivity with respect to spontaneous Raman. Up to now, CARS microscopy has been mainly employed to image the distribution of CH-stretching vibration,[94–96] offering a large potential for both *ex vivo*[97–99] and *in vivo* imaging[100,101] through its specificity in imaging lipids. In addition, CARS is used for imaging other relevant biological molecules such as DNA or proteins.[102,103]

Even if the capabilities of multimodal NLO microscopy for diagnostic purposes have been already largely demonstrated, the cost and the complexity of the equipment has restricted so far the use to technological research laboratories. Nevertheless, in the near future, these complex microscopic setups could find place in the mainstream biomedical, biochemical and clinical research laboratories. In this review paper, after having provided a detailed introduction on morphological and functional NLO microscopy techniques, we describe some applications of these techniques to tissue imaging. Starting from applications involving morphological imaging using TPF microscopy, we then present relevant applications employing a multimodal NLO microscopy approach on both arterial and skin tissue. In the last part, we summarize conclusion and potential future application of multimodal NLO microscopy.

2. Results and Discussion

2.1. *Morphological imaging of epithelial cells using TPF microscopy*

TPF microscopy is extremely powerful for label-free imaging with sub-cellular resolution of cells in a biological tissue and for investigating cellular morphology. In fact, TPF microscopy can take advantage of the endogenous fluorescence of mitochondrial NADH to excite a strong signal from cellular cytoplasm. Morphological features of the epithelium can be highlighted on both living tissue *in situ* or on fresh tissue biopsies up to 2–3 h from excision.[14,104] In this example, TPF imaging is

performed on fresh human colon biopsies using an excitation wavelength of 740 nm, adequate for exciting NADH fluorescence. Similar studies employing SHG microscopy were already carried out.[105,106] Thick tissue samples are optically sectioned with sub-cellular resolution using TPF microscopy. Figure 1 shows the comparison between TPF images acquired in different samples of fresh human colon biopsies using TPF microscopy and histological images taken after histopathological examination of the same samples. The good agreement between TPF and histological images confirms the capability of TPF microscopy for highlighting morphological features of tissues in a noninvasive label-free manner. The morphology of healthy colon mucosa [see Figs. 1(b) and 1(h)] consists of regularly packed cells with uniform size and fluorescence level that surround crypts. The correspondence with histological images [see Figs. 1(a) and 1(g)] is good. The cellular morphology is altered in adenomatous polyp [see Figs. 1(d) and 1(k)] which shows cells having a more elongated shape and nuclei. Similar observations can be performed by looking at the corresponding histological images [see Figs. 1(c) and 1(j)]. Adenocarcinoma [see Figs. 1(f) and 1(m)] exhibits a completely different cellular morphology, characterized by the proliferation of complex glandular structures and by large and stratified cellular nuclei. The less regular shape of adenocarcinoma with respect to the other samples affects the correspondence with histological images [see Figs. 1(e) and 1(l)] that show a reduced agreement with TPF images. A detailed analysis of cellular morphology can be performed by analyzing high-resolution.

TPF images of cells. From the acquired images it is possible to distinguish an altered cellular shape in adenomatous polyp [see Fig. 1(o)] and a larger nuclear size in adenocarcinoma [see Fig. 1(p)], in comparison to healthy mucosa [see Fig. 1(n)]. Image processing including the application of a threshold and background removal allows evaluating both cellular and nuclear size in order to calculate geometrical parameters peculiar of each tissue type. A statistical analysis performed on a large number of cells allows calculating the average ratio of cellular to nuclear size and the average cellular asymmetry. A smaller ratio of cellular to nuclear size is found for adenocarcinoma compared to both adenomatous and healthy tissues [see Fig. 1(q)]. This feature is considered a typical signature of malignancy. In

fact, it has already been measured by means of TPF microscopy in malignant cells of bladder,[108] and skin.[109,110] The average ratio measured in each tissue type, with standard deviation taken as error, is reported in Fig. 1(q). Further characterization can be obtained by considering the cellular asymmetry. In fact, nuclear elongation is a typical feature of adenomatous polyp. The average cellular asymmetry values, calculated based on the ratio between major and minor axis of the cells, are plotted in a graph in Fig. 1(r), showing a higher ratio for adenomatous polyp compared to both healthy mucosa and adenocarcinoma. This morphological analysis could be easily applied to TPF images taken from other tissues, since NADH is found in every epithelium. Extending this approach to other inflammatory and dysplastic tissue conditions could open the possibility to use the method for diagnosing tumors ina very early stage.

2.2. *Multimodal NLO microscopy: Imaging of collagen and cholesterol using combined SHG and CARS*

In this paragraph, we describe an application of NLO microscopy aimed at characterizing atherosclerotic arterial tissue. In particular, thin slices of arterial tissue from an animal model for atherosclerosis are imaged using combined SHG and CARS microscopy. The combined imaging approach allows selectively imaging various tissue components. Few examples of combined SHG-CARS imaging are provided in Figs. 2(a)–2(i), where images obtained from a thin arterial cross section of rabbit aorta are shown. Regions with different level of atherosclerotic plaques deposition are shown in the images contained in the first row [see Figs. 2(a)–2(c)]. The possibility of selectively targeting different components using different contrast mechanisms is demonstrated in the rows beneath. CARS microscopy, tuned in resonance with CH-stretching provides a strong signal from lipids within plaques and from proteins in the normal arterial wall [see Figs. 2(d)–2(f)]. SHG microscopy [see Figs. 2(g)–2(i)] provides high-contrast high-resolution background-free images of collagen in the normal arterial wall and cholesterol within plaques. Only recently,[111] SHG was proven useful for imaging cholesterol in atherosclerotic depositions. Hence, SHG microscopy can be used for
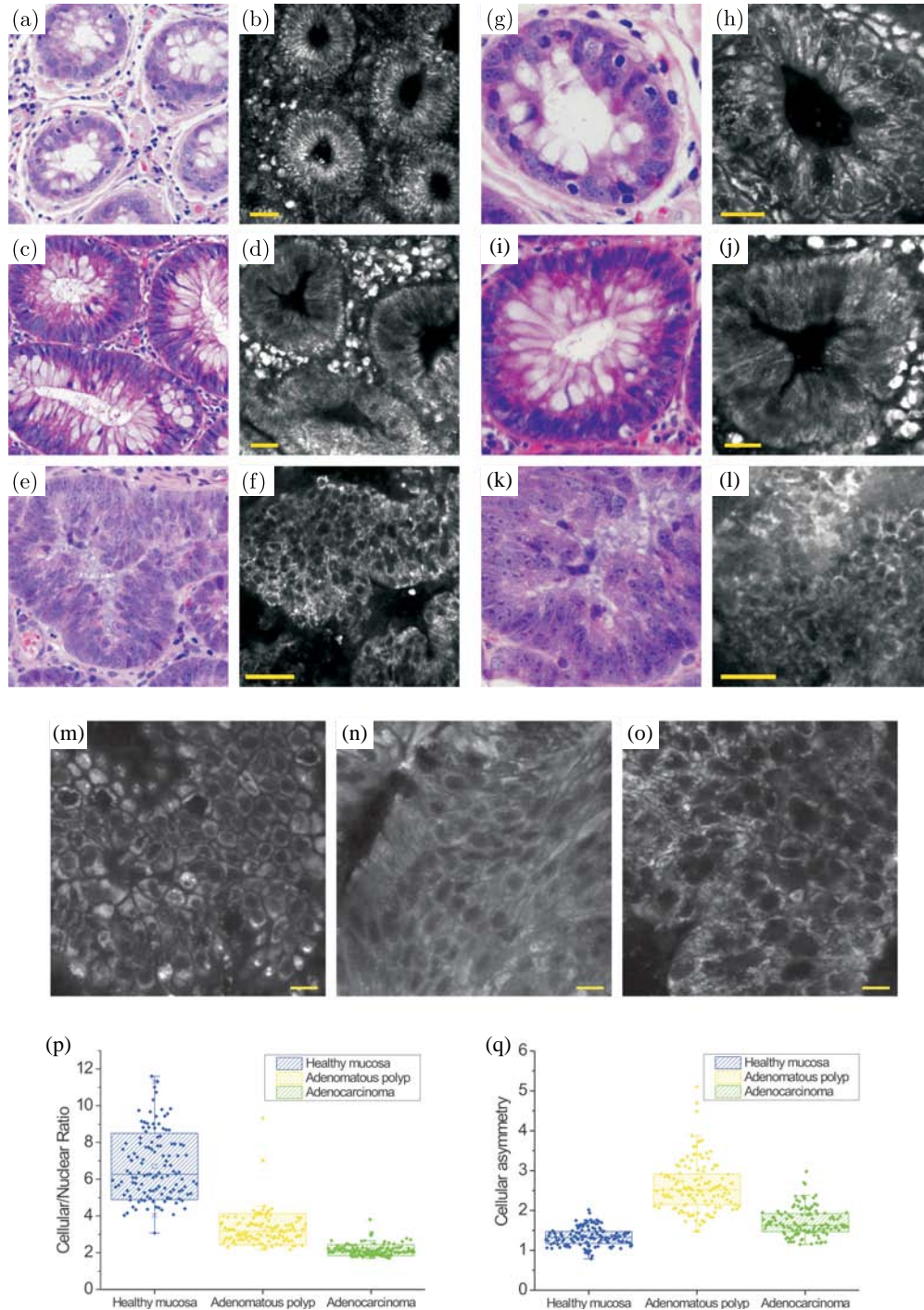
Fig. 1. Histological images taken using a 20X objective on H&E stained tissue sections of healthy colon mucosa (a), adenomatous polyp (c), and adenocarcinoma (e). Corresponding TPF images (taken with a 20X objective–0.9 NA) acquired from *ex vivo* fresh biopsies of healthy colon mucosa (b), adenomatous polyp (d) and adenocarcinoma (f). Scale bars: 40 μm. Histological images taken using a 40X objective on H&E stained tissue sections of healthy colon mucosa (g), adenomatous polyp (i), and adenocarcinoma (k). Corresponding TPF images (taken with a 40X objective – 1.3 NA) acquired from *ex vivo* fresh biopsies of healthy colon mucosa (h), adenomatous polyp (j) and adenocarcinoma (l). Scale bars: 30 μm. TPF images at high resolution (taken with a 40X objective — 1.3 NA) of healthy colon mucosa (m), adenomatous polyp (p) and adenocarcinoma (o) acquired at 30 μm depth from tissue surface on *ex vivo* fresh biopsies. Scale bars: 10 μm. (p) Distribution of the cellular/nuclear size ratio for healthy mucosa, adenomatous polyp and adenocarcinoma. (q) Distribution of the cellular asymmetry for healthy mucosa, adenomatous polyp and adenocarcinoma. In the graphs, dots represent single data points, while the box is enclosing the data within standard deviation. Figure modified from Ref. 107.
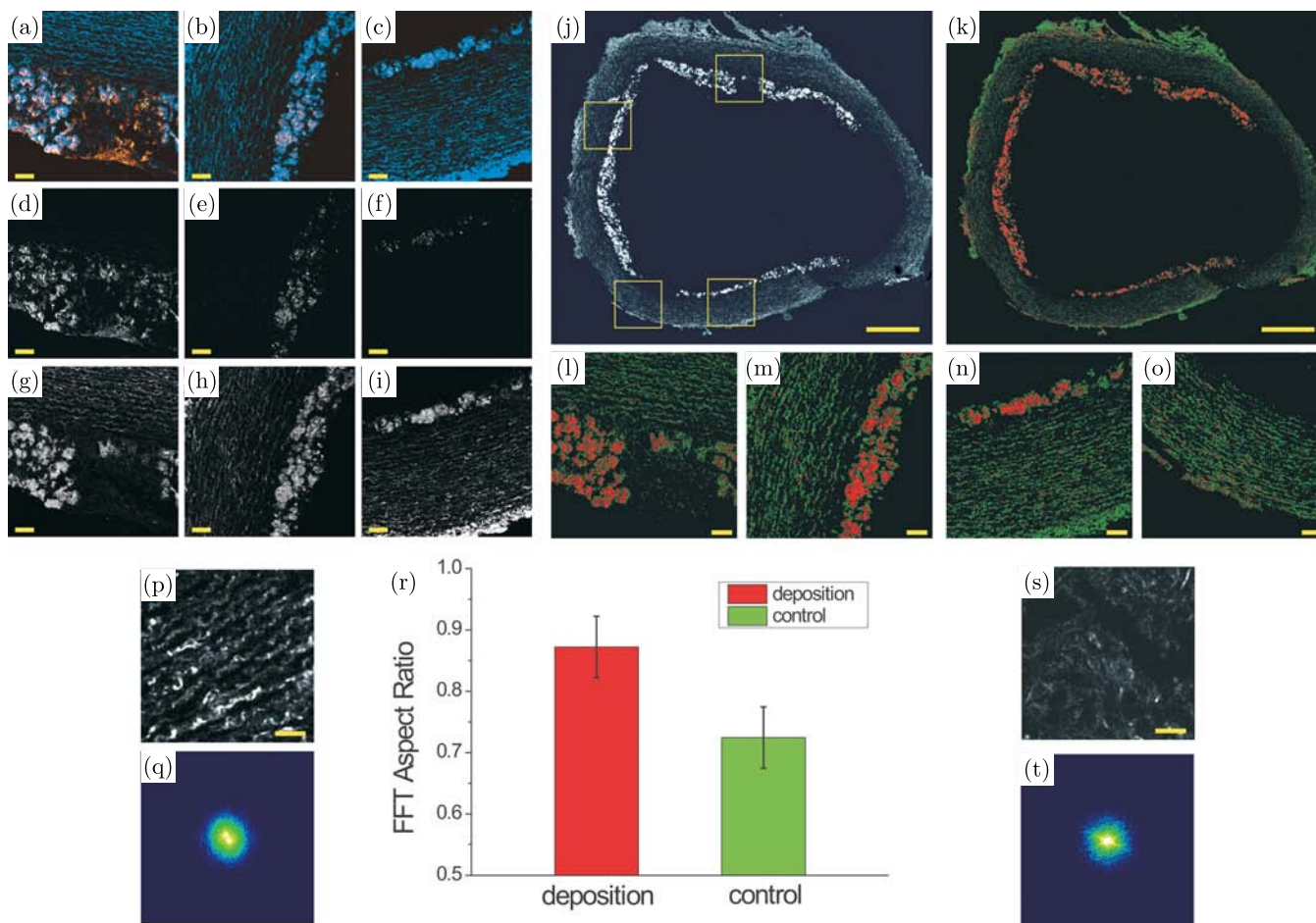
Fig. 2.   Combined SHG-CARS nonlinear images of thin atherosclerotic arterial tissue sections from rabbit aorta. (a)–(c) Images showing a color merge of SHG (blue) and CARS (orange), acquired in regions with a different level of plaque deposition. On the lower rows CARS (g)–(i) and SHG (d)–(f) are presented separately. Scale bars: $20\,\mu$m. Tissue regions represented in images (a), (b) and (c), correspond to the regions represented in images (l), (m) and (n), respectively. (j) Combined F-SHG and B-SHG image of a thin cross section of rabbit aorta with atherosclerotic plaque depositions. (k) Color map coding for the F/B SHG ratio in a color coded scale. Black: F/B < 1. Green: $1.5 <$ F/B < 2.5. Red: F/B > 4. Scale bars: $0.5\,$mm. Magnified details of a region with high (l), mild (m), low (n) and no (o) plaque deposition. The images in (l)–(o) correspond to the regions indicated by yellow squares in (j). Scale bars: $20\,\mu$m. SHG image of collagen within a control region (p) and a region with plaque depositions (s) with the corresponding FFT-images (q)–(t). Scale bars: $20\,\mu$m. (r) Histogram distribution of the average Fast Fourier Transform (FFT) aspect ratio within control and deposition regions. Figure modified from Ref. 114.

simultaneously imaging both collagen and cholesterol. However, the characterization of atherosclerotic arterial tissue requires the capability of separating the two contributions and discriminating the two molecules. The discrimination of collagen from cholesterol could open novel possibilities for SHG to be used for tissue diagnostics. One possibility is offered by the coherence properties of SHG light. Since SHG preserves both energy and momentum, the emission pattern, and particularly the amount of forward and backward scattered SHG (F-SHG and B-SHG), strongly depends on:

the spatial extent of the emission source[112]; the angle between the excitation field and the molecular emitters[14]; the axial periodicity of the emitters.[113] Hence, the simultaneous detection of F-SHG and B-SHG could be used for inferring information on the spatial distribution of SHG emitters within the focal volume.[39,82] In this example, the measurement of the ratio of forward over backward SHG signal (F/B-SHG) allows discriminating cholesterol in the arterial lumen from collagen in the arterial wall, as shown in Figs. 2(j)–2(o). Figure 2(j) shows an image of an arterial thin cross sectioned slice,

obtained by summing the SHG signal detected forward and backward. A strong signal, probably due to cholesterol, originates from plaque deposition, whereas the signal from collagen found in the normal arterial wall is lower. Hence, these two tissue regions can be distinguished based only on the SHG intensity. The problem related with this approach is that collagen intermixed with cholesterol within plaques cannot be resolved unless the F/B SHG ratio analysis is performed. In fact, the measurement of the F/B SHG ratio allows discriminating collagen from cholesterol since a higher F/B value is found in cholesterol (4 to 10) than in collagen (1.5 to 2.5), as demonstrated by the F/B SHG ratio map in Fig. 2(k). Multi-thresholds are applied to the image in order to obtain a black background (F/B < 1), green collagen (1.5 < F/B < 2.5) and red cholesterol (F/B > 4). The capabilities of the method are clear when observing the regions with different levels of deposition [see Figs. 2(l)–2(o)], where cholesterol (in red) is found intermixed with collagen (in green) within the atherosclerotic plaques. The choice of colors with high chromatic contrast highlights the discrimination capability. This separating procedure allows conducting further analysis on collagen organization in the two tissue regions (normal wall and atherosclerotic plaques). Collagen fibers are organized in equally spaced fiber bundles with a wave-like shape in the normal arterial wall. On the other hand, collagen found within plaques shows randomly oriented disorganized fibers. FFT analysis [see Fig. 2(p)–2(t)] can be used to characterize the isotropy-anisotropy distribution of collagen fiber bundles through the measurement of the aspect ratio of the FFT profile. As expected, the FFT aspect ratio has a lower value in normal tissue (more anisotropic) with respect to the atherosclerotic plaques (more isotropic). The average fiber bundle size and spacing in the two tissue regions can be determined using gray-level co-occurrence matrix (GLCM) analysis, as reported in Ref. 114. The mean fiber bundle size is found higher in the normal arterial wall with respect to the atherosclerotic plaques. The architectural features of collagen highlighted by this technique could be related to plaque vulnerability. Hence, this analysis using SHG represents a valid label-free diagnostic alternative to standard histopathological methods for evaluating atherosclerotic arterial tissue and has the potential to be used for determining plaque vulnerability.

2.3. *Multimodal NLO microscopy: Imaging of skin cancer using combined TPF, SHG and CARS*

The main aim of using multiple NLO microscopy techniques in combination consists of highlighting different tissue components by taking advantage of the specific contrast provided by each imaging technique. As pointed out in the introduction, morphological information on cells and collagen can be provided by TPF and SHG microscopy, respectively, whereas Raman-based techniques allows for a more detailed characterization of the chemical-molecular composition of the tissue under investigation.[89,115,116] Hence, combining TPF and SHG microscopy with CARS microscopy allows providing both morphological and chemical information in tandem, realizing a morpho-chemical characterization of a biological specimen. The implementation of all these techniques in the same experimental setup is straightforward since the pump (or the Stokes) pulses for CARS can be used for exciting TPF and SHG. In this paragraph, we report the results obtained by combining morphological and functional NLO microscopy techniques in a multi-modal morpho-chemical approach. Such approach is used with the aim of characterizing the morpho-chemistry of basal cell carcinoma (BCC), demonstrating the capability of the method in providing a full description of the morpho-chemistry of BCC. Further, this example represents a first benchmark for future applications of the same technique to other biological tissues. An example of multimodal NLO microscopy is shown in Fig. 3, where a thin section of BCC is imaged using TPF, SHG and CARS and compared to the histological image taken from an adjacent tissue slice. As shown in Fig. 3(a), TPF microscopy highlights cellular morphology in a good agreement with corresponding histology. BCC is characterized by cell nests and by a higher nucleus to cytoplasm ratio, which is typical of malignant cells. These two features could help in discriminating tumor from normal healthy tissue. In comparison with histological examination, where malignant cells are identified only based on their large nuclei, multimodal NLO microscopy allows to take into account other relevant features, such as the tightly packed cytoplasm of malignant cells or the organization of collagen surrounding cell nests. In this region, collagen plays a crucial role during tumor growth and proliferation[117] and it can be
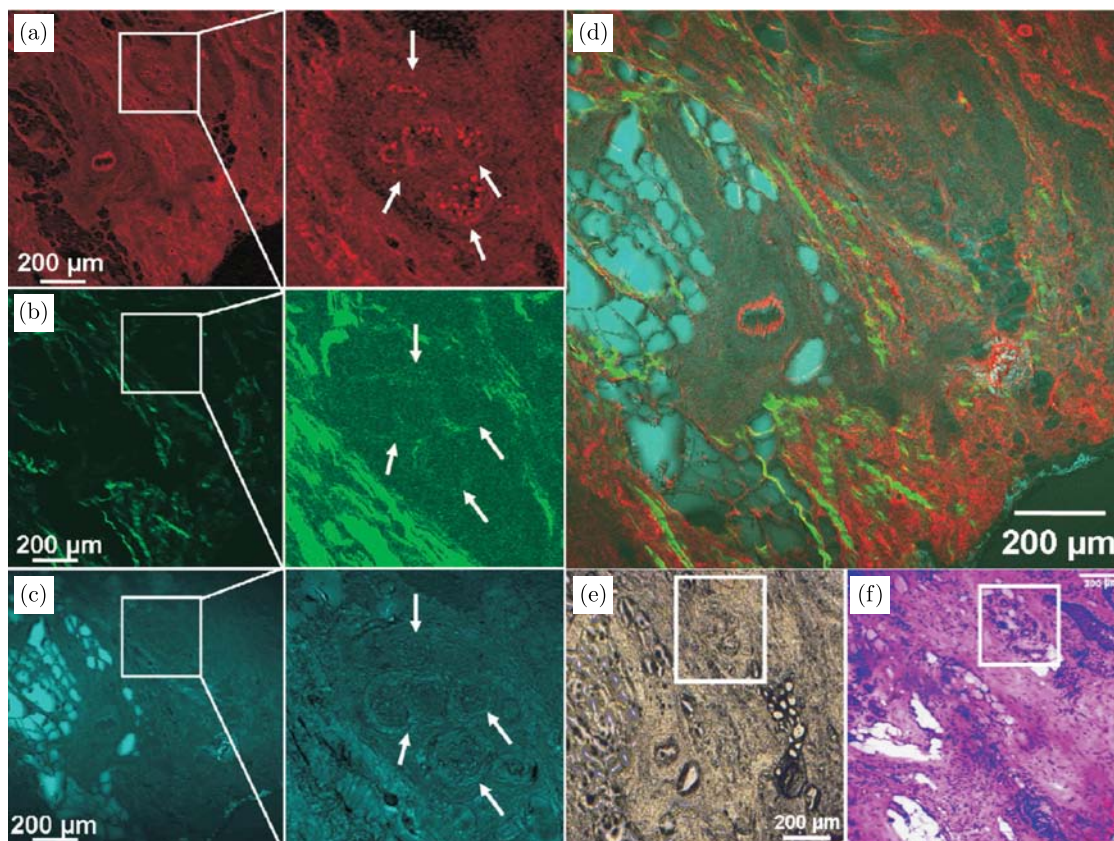
Fig. 3. Multimodal TPF-SHG-CARS imaging. (a) TPF images (coded in red) highlighting dominantly fluorescing proteins and cofactors. (b) SHG images (coded in green) showing collagen distribution. (c) Fat reservoirs as well as membranes visualized with CARS microscopy (coded in cyan). In all three images the tumor can be found (indicated by the arrows). (d) Multimodal image of BCC obtained by merging individual images. (e) Bright field image with the tumor area indicated by the white box. (f) Histological H&E stained image for comparison. The tumor area is indicated by the white box. Figure modified from Ref. 118.

imaged using SHG microscopy. As shown in Fig. 3 (B), collagen surrounding cell nests (arrows) is characterized by a lower signal, compared to the collagen located in other regions where it surrounds the elongated tumor lobes. Although it is not straightforward interpreting SHG intensity variations in terms of collagen organization within the focal volume, it is evident that collagen organization is quite different in the two regions. In particular, with SHG microscopy it is possible to exclusively image collagen that was not denatured by the interaction with collagenase released by proliferating cells. Even if not completely denatured, the different intensity level of SHG originating from collagen surrounding cell nests is probably due to a different supramolecular organization of collagen in this region, compared to a normal collagen. This method was firstly employed in studies aimed at characterizing collagen fibers surrounding a tumor lesion.[66,73,80] CARS microscopy allows direct label-free imaging of the tumor by taking advantage of the strong signal originating from CH-stretching vibrations. In particular, tuning pump and Stokes frequency difference in resonance with CH-stretching vibrations, CARS microscopy allows visualizing a signal dominated by the contribution from lipids. The use of CARS microscopy as a lipid-sensitive technique allowed to observe for the first time a large fat reservoir in BCC [see Fig. 3(c)].[118] In particular, the amount of fat-rich cells in BCC tissue is significantly high. The authors hypothesize that the role of these cells is to provide nutrition for proliferating cells, even if this finding is not verified yet. A big advantage related to the multimodal NLO approach is the possibility to implement image-processing algorithm on digital images. As pointed out in Secs. 2.1 and 2.2 for TPF images of cells and SHG images of collagen, images can be quantitatively analyzed in terms of cellular and collagen morphology and organization. Here we describe an additional example of image

processing on CARS images, aimed at quantifying the size of fat droplets observed in fat-containing cells using a watershed algorithm.[119] The average diameter of fat-containing cells was evaluated to be 55 μm. Such value can be affected by the level of threshold used and by possible artifacts introduced by tissue slicing. Nevertheless, it provides quantitative measurement of fat droplets found in BCC. Despite these and other limitations of multimodal NLO microscopy, the agreement of the images with histological images is impressive, as demonstrated in Fig. 3(f). Compared to common routine histology, the multimodal NLO approach provides: higher spatial resolution; better contrast; highlighting of more tissue constituents; a label-free modality; a quantitative analysis providing objective metric as opposed to a judgment by a clinician performing histological analysis. Considering all the above-mentioned advantages, multimodal NLO microscopy has the potential to define a new standard for tissue classification.

3. Discussion

In the previous sections, we deeply described the advantages and potentials offered by multimodal NLO microscopy in terms of diagnostic capabilities on *ex vivo* tissues, while here we discuss disadvantages, limitations and drawbacks of the method, especially in relationship to the *in vivo* imaging implementation. *In vivo* imaging using multimodal NLO microscopy has already been largely demonstrated on skin,[21,120] which is easily accessible from the optical point of view. Imaging other tissues, such as internal tissues and hollow organs, is much more challenging, considering the fact that laser scanning imaging needs to be implemented in an endoscopic probe. Currently, there is a big challenge to setup NLO microscopy in modern endoscopes. In the last years, several developments were done in the field of confocal endoscopy, giving rise to a growing number of research instruments and also to few commercial flexible endoscopes. Both confocal microscopy[121] and endoscopy[122] have already been used for imaging tissue samples. New technologies for scanning systems miniaturization (MEMS, ultra-sound scanning devices), for pulse delivery optimization (PCF, hollow-core fibers) as well as for miniaturization of high-NA optics (GRIN-lenses) have created new insights for both single and multi-photon endoscopic imaging. SHG endoscopic imaging has

already been performed *in vivo* by means of a rigid needle with a GRIN-lens optically coupled to the microscope objective.[123] In the last years, a flexible two-photon endoscope has been developed and successfully used on the animal model.[124,125] According to the capabilities that NLO imaging techniques have already been largely shown in providing "optical biopsy" of a tissue, in the near future NLO endoscopy would represent a breakthrough in various medical fields for both early diagnosis and therapy follow-up. A critical feature for the *in vivo* implementation of these imaging techniques is related to the radiation dose deposited within the tissue under examination and its side effects. Few years ago, a study aimed at measuring the amount of ROS generated in skin after two-photon laser imaging demonstrated that the amount of ROS induced by Ti:Sa laser irradiation with a typical acquisition is comparable to the effect of few hours under sun.[126] More studies that have recently examined the risk of carcinogenetic effect on DNA following NLO imaging[127,128] found that both two- and three-photon absorption processes have a potential carcinogenetic effect on DNA, similar to the UV exposure. In fact, in terms of energy deposed, both two- and three-photon absorption of NIR photons are equivalent to the absorption of a single photon in the UV range. Even if several studies, including a larger number of samples have to be conducted for deriving conclusion, there is a risk associated with *in vivo* NLO imaging. We think that a proper evaluation of the benefit-risk ratio should be done when using the technique *in vivo*, as is normally done for other imaging diagnostic techniques such as X-ray or CT, which are not risk free.

Other limitations can be related to the *in vivo* implementation of the diagnostic methods presented in Sec. 2. Regarding the use of NADH fluorescence for highlighting both cellular morphology and functionality, there are some limitations related to the examination of *ex vivo* tissues, especially for what is concerning tissue metabolic activity. As already pointed out previously, even if tissue degradation starts immediately after excision, NADH and FAD can be found in tissue and used for intrinsic imaging up to 2–3 h after excision.[14,104] Hence, they can be used for imaging tissue morphology. Functional imaging of the metabolic state is also possible but the measurement is affected by the time between excision and imaging, and is

limited to the relative abundance of the two nucleotides,[107,108] whereas a functional metabolic imaging, aimed at investigating the amount of free and bound NADH, is possible only *in vivo*. In fact, in living tissue, free and bound NADH abundance can be determined optically by means of time[129] or spectral-resolved measurements of NADH fluorescence.[130] Alteration of the normal value of free-to-bound NADH can be taken as an indicator of altered metabolic activity, which can be in turn related to pathologic conditions.

Regarding SHG microscopy, we presented the potential offered by this coherent technique for determining the organization of emitters within the focal volume. In particular, we demonstrated the capability of F/B SHG ratio for discriminating collagen from cholesterol. Although this method is extremely powerful and can be extended to the examination of various molecular SHG emitters, its *in vivo* implementation is not straightforward. In fact, simultaneous F/B detection of SHG is in principle prevented *in vivo* because of a mandatory epi-detection geometry. Nevertheless, F-SHG and B-SHG could be discriminated based on polarization. In fact, for a linearly polarized excitation, B-SHG maintains a linear polarization, whereas F-SHG, detected after multiple scattering events in the underlying tissue, will be depolarized. Hence, upon some limitations with respect to the *ex vivo* approach, the two contributions could be in principle detected using a crossed polarization detection approach and a proper image processing. A more effective approach for discriminating F-SHG and B-SHG in epi-detection geometry has been recently proposed by Han and co-workers.[131] In particular, the authors employed a confocal detection allowing the selective detection of B-SHG, removing F-SHG from the detected signal. Using this approach, it is possible to detect F/B SHG ratio also in epi-detection and hence *in vivo*. The only drawback is that the measurement is not simultaneous but it requires two distinct measurements (one with and one without pinhole) as well as image post-processing.

4. Conclusion

In conclusion, during the last years NLO microscopy has gained enormous momentum in biomedical optics by providing label-free high-resolution imaging in deep tissue. A broad variety of techniques, aimed at highlighting morphological and functional features of tissues have been developed and successfully applied to tissue imaging. Additional advantages are provided by the combined application of multiple techniques. Multimodal NLO microscopy represents today a powerful research tool for label-free imaging and classification of both *ex vivo* and *in vivo* tissues. According to the results obtained on tissue diagnostics, the method has the potential to set a new standard aside from the "gold standard" represented by histopathological examination. Further, considering the recent developments in NLO endoscopy, the method could be extended to a broader range of clinical diagnostic problems.

Acknowledgments

References

1. W. R. Zipfel, R. M. Williams, W. W. Webb, "Nonlinear magic: Multiphoton microscopy in the biosciences," *Nat. Biotechnol.* **21**, 1369–1377 (2003).
2. F. Helmchen, W. Denk, "Deep tissue two-photon microscopy," *Nat. Methods.* **2**, 932–940 (2005).
3. V. E. Centonze, J. G. White, "Multiphoton excitation provides optical sections from deeper within scattering specimens than confocal imaging," *Biophys. J.* **75**, 2015–2022 (1998).
4. M. Goppert-Mayer, "Uber elementarekte mit zwei Quantensprunger," *Ann. Phys.* **9**, 273 (1931).
5. W. Denk, H. J. Strickler, W. W. Webb, "Two-photon laser scanning fluorescence microscope," *Science* **248**, 73–76 (1990)
6. R. M. Williams, W. R. Zipfel, W. W. Webb, "Multiphoton microscopy in biological research," *Curr. Opin. Chem. Biol.* **5**, 603–608 (2001).
7. K. König, "Multiphoton microscopy in life sciences," *J. Microsc.* **200**, 83–104 (2000).
8. S. Huang, A. A. Heikal, W. W. Webb, "Two-photon fluorescence spectroscopy and microscopy of NAD(P)H and flavoprotein," *Biophys. J.* **82**, 2811–2825 (2002).

9. A. Volkmer, V. Subramaniam, D. J. S. Birch, T. M. Jovin, "One and two-photon excited fluorescence lifetimes and anisotropy decays of green fluorescent proteins," *Biophys. J.* **78**, 1589–1598 (2000).

10. C. Xu, W. Zipfel, J. B. Shear, R. M. Williams, W. W. Webb, "Multiphoton fluorescence excitation: New spectral windows for biological nonlinear microscopy," *Proc. Natl. Acad. Sci. USA* **93**, 10763–10768 (1996).

11. M. Rubart, E. Wang, K. W. Dunn, L. J. Field, "Two-photon molecular excitation imaging of Ca^{2+} transients in Langendorff-perfused mouse hearts," *Am. J. Physiol. Cell Physiol.* **284**, C1654–C1668 (2003).

12. M. Oheim, E. Beaurepaire, E. Chaigneau, J. Mertz, S. Charpak, "Two-photon microscopy in brain tissue: Parameters influencing the imaging depth," *J. Neurosci. Methods* **111**, 29–37 (2001).

13. A. Zoumi, A. T. Yeh, B. J. Tromberg, "Imaging cells and extracellular matrix in vivo by using second-harmonic generation and two-photon excited fluorescence," *Proc. Natl. Acad. Sci. USA* **99**, 11014–11019 (2002).

14. W. R. Zipfel, R. M. Williams, R. Christie, A. Y. Nikitin, B. T. Hyman, W. W. Webb, "Live tissue intrinsic emission microscopy using multiphoton-excited native fluorescence and second harmonic generation," *Proc. Natl. Acad. Sci. USA* **100**, 7075–7080 (2003).

15. B. R. Masters, P. T. C. So, E. Gratton, "Multiphoton excitation fluorescence microscopy and spectroscopy of in vivo human skin," *Biophys. J.* **72**, 2405–2412 (1997).

16. B. R. Masters, P. T. C. So, E. Gratton, "Optical biopsy of in vivo human skin: Multi-photon excitation microscopy," *Lasers Med. Sci.* **13**, 196–203 (1998).

17. B. R. Masters, P. T. C. So, "Confocal microscopy and multi-photon excitation microscopy of human skin in vivo," *Opt. Express* **8**, 2–9 (2001).

18. K. Konig, I. Riemann, "High-resolution multiphoton tomography of human skin with subcellular spatial resolution and picosecond time resolution," *J. Biomed. Opt.* **8**, 432–439 (2003).

19. F. Helmchen, W. Denk, "Deep tissue two-photon microscopy," *Nat. Methods.* **2**(12), 932–940 (2005).

20. K. Svoboda, R. Yasuda, "Principles of two-photon excitation microscopy and its applications to neuroscience," *Neuron* **50**(6), 823–839 (2006).

21. K. Konig, "Clinical multiphoton tomography," *J. Biophotonics* **1**(1), 13–23 (2008).

22. M. J. Koehler, K. König, P. Elsner, R. Buckle, M. Kaatz, "In vivo assessment of human skin aging by multiphoton laser scanning tomography," *Opt. Lett.* **31**, 2879–2881 (2006).

23. E. Dimitrow, I. Riemann, A. Ehlers, M. J. Koehler, J. Norgauer, P. Elsner, K. Konig, M. Kaatz, "Spectral fluorescence lifetime detection and selective melanin imaging by multiphoton laser tomography for melanoma diagnosis," *Exp. Dermatol.* **18**(6), 509–515 (2009).

24. J. N. Gannaway, C. J. R. Sheppard, "Second-harmonic imaging in the scanning optical microscope," *Opt. Quant. Elect.* **10**, 435–439 (1978).

25. C. J. R. Sheppard, R. Kompfner, J. Gannaway, D. Walsh, "Scanning harmonic optical microscope," *IEEE J. Quantum Electron.* **13E**, 100D (1977).

26. R. Cicchi, L. Sacconi, F. Vanzi, F. S. Pavone, "How to build an SHG apparatus, in *Second-Harmonic Generation Imaging*," F. S. Pavone, P. J. Campagnola, Eds., CRC Press (2013).

27. S. Fine, W. P. Hansen, "Optical second harmonic generation in biological systems," *Appl. Opt.* **10**, 2350–2353 (1971).

28. W. A. Mohler, A. C. Millard, P. J. Campagnola, "Second harmonic generation imaging of endogenous structural proteins," *Methods* **29**, 97–109 (2003).

29. S. Roth, I. Freund, "Second harmonic generation in collagen," *J. Chem. Phys.* **70**, 1637–1643 (1979).

30. I. Freund, M. Deutsch, A. Sprecher, "Optical second-harmonic microscopy, crossed-beam summation and small-angle scattering in rat-tail tendon," *Biophys. J.* **50**, 693–712 (1986).

31. R. Cicchi, N. Vogler, D. Kapsokalyvas, B. Dietzek, J. Popp, F. S. Pavone, "From molecular structure to tissue architecture: Collagen organization probed by SHG microscopy," *J. Biophoton.* **6**, 129–142 (2012).

32. M. Both, M. Vogel, O. Friedrich, F. Von Wegner, T. Kunsting, R. H. A. Fink, D. Uttenweiler, "Second harmonic imaging of intrinsic signals in muscle fiber in situ," *J. Biomed. Opt.* **87**, 882–892 (2004).

33. T. Boulesteix, E. Beaurepaire, M. P. Sauviat, M. C. Schanne-Klein, "Second-harmonic microscopy of unstained living cardiac myocytes: Measurements of sarcomere length with 20 nm accuracy," *Opt. Lett.* **29**, 2031–2033 (2004).

34. M. E. Llewellyn, R. P. J. Barretto, S. L. Delp, M. J. Schnitzer, "Minimally invasive high-speed imaging of sarcomere contractile dynamics in mice and humans," *Nat. Lett.* **454**, 784–788 (2008).

35. V. Nucciotti, C. Stringari, L. Sacconi, F. Vanzi, L. Fusi, M. Linari, G. Piazzesi, V. Lombardi, F. S. Pavone, "Probing myosin structural conformation in vivo by second-harmonic generation microscopy," *Proc. Natl. Acad. Sci. USA* **107**, 7763–7768 (2010).

36. S. V. Plotnikov, A. C. Millard, P. J. Campagnola, W. A. Mohler, "Characterization of the myosin-

based source for second-harmonic generation from muscle sarcomeres," *Biophys. J.* **90**, 693–703 (2006).

37. F. Vanzi, L. Sacconi, R. Cicchi, F. S. Pavone, "Protein conformation and molecular order probed by second-harmonic generation microscopy," *J. Biomed. Opt.* **17**(6), 060901 (2012).

38. D. A. Dombeck, K. A. Kasischke, H. D. Vishwasrao, M. Ingelsson, B. T. Hyman, W. W. Webb, "Uniform polarity microtubule assemblies imaged in native brain tissue by second-harmonic generation microscopy," *Proc. Natl. Acad. Sci. USA* **100**, 7081–7086 (2003).

39. R. Cicchi, N. Vogler, D. Kapsokalyvas, B. Dietzek, J. Popp, F. S. Pavone, "From molecular structure to tissue architecture: Collagen organization probed by SHG microscopy," *J. Biophoton.* **6**, 129–142 (2013).

40. P. J. Campagnola, M. D. Wei, A. Lewis, L. M. Loew, "High-resolution nonlinear optical imaging of live cells by second harmonic generation," *Biophys. J.* **77**, 3341–3349 (1999).

41. T. Pons, L. Moreaux, O. Mongin, M. Blanchard-Desce, J. Mertz, "Mechanisms of membrane potential sensing with second-harmonic generation microscopy," *J. Biomed. Opt.* **8**, 428–431 (2003).

42. A. Zoumi, A. Yeh, B. J. Tromberg, "Imaging cells and extracellular matrix in vivo by using second harmonic generation and two-photon excited fluorescence," *Proc. Natl. Acad. Sci. USA* **99**, 11014–11019 (2002).

43. P. J. Campagnola, L. M. Loew, "Second-harmonic imaging microscopy for visualizing biomolecular arrays in cells, tissues and organisms," *Nat. Biotechnol.* **21**, 1356–1360 (2003).

44. J. Mertz, L. Moreaux, "Second-harmonic generation by focused excitation of inhomogeneously distributed scatterers," *Opt. Commun.* **196**, 325–330 (2001).

45. L. Moreaux, O. Sandre, S. Charpak, M. Blanchard-Desce, J. Mertz, "Coherent scattering in multi-harmonic light microscopy," *Biophys. J.* **80**, 1568–1574 (2001).

46. L. Moreaux, O. Sandre, J. Mertz, "Membrane imaging by second-harmonic generation microscopy," *J. Opt. Soc. Am. B* **17**, 1685–1694 (2000).

47. L. Moreaux, O. Sandre, M. Blanchard-Desce, J. Mertz, "Membrane imaging by simultaneous second-harmonic generation and two-photon microscopy," *Opt. Lett.* **25**, 320–322 (2000).

48. P. J. Campagnola, A. C. Millard, M. Terasaki, P. E. Hoppe, C. J. Malone, W. A. Mohler, "Three-dimensional high-resolution second-harmonic generation imaging of endogenous structural proteins in biological tissues," *Biophys J.* **81**, 493–508 (2002).

49. Y. Guo, P. P. Ho, H. Savage, D. Harris, P. Sacks, S. Schantz, F. Liu, N. Zhadin, R. R. Alfano, "Second-harmonic tomography of tissues," *Opt. Lett.* **22**, 1323–1325 (1997).

50. G. Cox, E. Kable, A. Jones, I. Fraser, F. Manconi, M. D. Gorrell, "Three dimensional imaging of collagen using second harmonic generation," *J. Struct. Biol.* **141**, 53–62 (2003).

51. M. Han, G. Giese, J. F. Bille, "Second harmonic generation imaging of collagen fibrils in cornea and sclera," *Opt. Express.* **13**, 5791–5797 (2005).

52. A. Yeh, N. Nassif, A. Zoumi, B. J. Tromberg, "Selective corneal imaging using combined second harmonic generation and two-photon excited fluorescence," *Opt. Lett.* **27**, 2082–2084 (2002).

53. P. Stoller, B. M. Kim, A. M. Rubenchik, K. M. Reiser, L. B. Da Silva, "Polarization-dependent optical second-harmonic imaging of a rat-tail tendon," *J. Biomed. Opt.* **7**(2), 205–214 (2002).

54. T. Theodossiou, C. Thrasivoulou, C. Ekwobi, D. Becker, "Second harmonic generation confocal microscopy of collagen type I from rat tendon cryosections," *Biophys J.* **91**, 4665–4677 (2006).

55. A. Zoumi, X. Lu, G. S. Kassab, B. J. Tromberg, "Imaging coronary artery microstructure using second-harmonic and two-photon fluorescence microscopy," *Biophys. J.* **87**, 2778–2786 (2004).

56. P. Stoller, K. M. Reiser, P. M. Celliers, A. M. Rubenchik, "Polarization-modulated second harmonic generation in collagen," *Biophys. J.* **82**, 3330–3342 (2002).

57. T. Yasui, Y. Tohno, T. Araki, "Characterization of collagen orientation in human dermis by two-dimensional second-harmonic-generation polarimetry," *J. Biomed. Opt.* **9**, 259–264 (2004).

58. P. J. Su, W. L. Chen, J. B. Hong, T. H. Li, R. Wu, C. K. Chou, S. J. Chen, C. Hu, S. J. Lin, C. Y. Dong, "Discrimination of collagen in normal and pathological skin dermis through second-order susceptibility microscopy," *Opt. Express* **17**, 11161–11171 (2009).

59. R. Cicchi, S. Sestini, V. De Giorgi, D. Massi, T. Lotti, F. S. Pavone, "Nonlinear laser imaging of skin lesions," *Journal of Biophotonics* **1**(1), 62–73 (2008).

60. A. Pena, D. Fagot, C. Olive, J. F. Michelet, J. B. Galey, F. Leroy, E. Beaurepaire, J. L. Martin, A. Colonna, M. C. Schanne-Klein, "Multiphoton microscopy of engineered dermal substitutes: Assessment of 3-D collagen matrix remodeling induced by fibroblast contraction," *J. Biomed. Opt.* **15**, 056018 (2010).

61. R. Cicchi, D. Kapsokalyvas, V. De Giorgi, V. Maio, A. Van Wiechen, D. Massi, T. Lotti, F. S. Pavone, "Scoring of collagen organization in healthy and diseased human dermis by multiphoton microscopy," *J. Biophoton.* **3**, 34–43 (2010).

62. J. Chen, S. Zhuo, X. Jiang, X. Zhu, L. Zheng, S. Xie, B. Lin, H. Zeng, "Multiphoton microscopy study of the morphological and quantity changes of collagen and elastic fiber components in keloid disease," *J. Biomed. Opt.* **16**, 051305 (2011).

63. A. Medyukhina, N. Vogler, I. Latka, S. Kemper, M. Böhm, B. Dietzek, J. Popp, "Automated classification of healthy and keloidal collagen patterns based on processing of SHG images of human skin," *J. Biophoton.* **4**, 627–636 (2011).

64. M. Strupler, A. M. Pena, M. Hernest, P. L. Tharaux, J. L. Martin, E. Beaurepaire, M. C. Schanne-Klein, "Second harmonic imaging and scoring of collagen in fibrotic tissues," *Opt. Express* **15**, 4054–4065 (2007).

65. T. Guilbert, C. Odin, Y. Le Grand, L. Gailhouste, B. Turlin, F. Ezan, Y. Désille, G. Baffet, D. Guyader, "A robust collagen scoring method for human liver fibrosis by second harmonic microscopy," *Opt. Express* **18**, 25794–25807 (2010).

66. L. Gailhouste, Y. Grand, C. Odin, D. Guyader, B. Turlin, F. Ezan, Y. Désille, T. Guilbert, A. Bessard, C. Fremin, N. Theret, G. Baffet, "Fibrillar collagen scoring by second harmonic microscopy: A new tool in the assessment of liver fibrosis," *J. Hepatol.* **52**, 398–406 (2010).

67. S. J. Lin, C. Y. Hsiao, Y. Sun, W. Lo, W. C. Lin, G. J. Jan, S. H. Jee, C. Y. Dong, "Monitoring the thermally induced structural transitions of collagen by use of second-harmonic generation microscopy," *Opt. Lett.* **30**, 622–624 (2005).

68. P. Matteini, F. Ratto, F. Rossi, R. Cicchi, C. Stringari, D. Kapsokalyvas, F. S. Pavone, R. Pini, "Photothermally-induced disordered patterns of corneal collagen revealed by SHG imaging," *Opt. Express* **17**(6), 4868–4878 (2009).

69. T. Theodossiou, G. S. Rapti, V. Hovhannisyan, E. Georgiou, K. Politopoulos, D. Yova, "Thermally induced irreversible conformational changes in collagen probed by optical second harmonic generation and laser-induced fluorescence," *Lasers Med Sci.* **17**, 34–41 (2002).

70. W. Lo, Y. L. Chang, J. S. Liu, C. M. Hseuh, V. Hovhannisyan, S. J. Chen, H. Y. Tan, C. Y. Dong, "Multimodal, multiphoton microscopy and image correlation analysis for characterizing corneal thermal damage," *J. Biomed. Opt.* **14**, 054003 (2009).

71. Y. Sun, W. L. Chen, S. J. Lin, S. H. Jee, Y. F. Chen, L. C. Lin, P. T. C. So, C. Y. Dong, "Investigating mechanisms of collagen thermal denaturation by high resolution second-harmonic generation imaging," *Biophys. J.* **91**, 2620–2625 (2006).

72. Y. Guo, H. E. Savage, F. Liu, S. P. Schantz, P. P. Ho, R. R. Alfano, "Subsurface tumor progression investigated by noninvasive optical second harmonic tomography," *Proc. Natl. Acad. Sci. USA* **96**, 10854–10856 (1999).

73. E. Brown, T. McKee, E. DiTomaso, A. Pluen, B. Seed, Y. Boucher, R. K. Jain, "Dynamic imaging of collagen and its modulation in tumors in vivo using second-harmonic generation," *Nat. Med.* **9**, 796–800 (2003).

74. S. J. Lin, S. H. Jee, C. J. Kuo, R. J. Wu, W. C. Lin, J. S. Chen, Y. H. Liao, C. J. Hsu, T. F. Tsai, Y. F. Chen, C. Y. Dong, "Discrimination of basal cell carcinoma from normal dermal stroma by quantitative multiphoton imaging," *Opt. Lett.* **31**, 2756–2758 (2006).

75. P. P. Provenzano, K. W. Eliceiri, J. M. Campbell, D. R. Inman, J. G. White, P. J. Keely, "Collagen reorganization at the tumor-stromal interface facilitates local invasion," *BMC Med.* **4**(1), 38–53 (2006).

76. X. Han, R. M. Burke, M. L. Zettel, P. Tang, E. B. Brown, "Second harmonic properties of tumor collagen: Determining the structural relationship between reactive stroma and healthy stroma," *Opt. Express.* **16**, 1846–1859 (2008).

77. A. M. Raja, S. Xu, W. Sun, J. Zhou, D. C. S. Tai, C. S. Chen, J. C. Rajapakse, P. T. C. So, H. Yu, "Pulse-modulated second harmonic imaging microscope quantitatively demonstrates marked increase of collagen in tumor after chemotherapy," *J. Biomed. Opt.* **15**, 056016 (2010).

78. O. Nadiarnykh, R. B. LaComb, M. A. Brewer, P. J. Campagnola, "Alteration of the extracellular matrix in ovarian cancer studied by second harmonic generation imaging microscopy," *BMC Cancer* **10**, 94 (2010).

79. S. V. Plotnikov, A. M. Kenny, S. J. Walsh, B. Zubrowski, C. Joseph, V. L. Scranton, G. A. Kuchel, D. Dauser, M. Xu, C. C. Pilbeam, D. J. Adams, R. P. Dougherty, P. J. Campagnola, W. A. Mohler, "Measurement of muscle disease by quantitative second-harmonic generation imaging," *J. Biomed. Opt.* **13**, 044018 (2008).

80. F. Vanzi, L. Sacconi, R. Cicchi, F. S. Pavone, "Molecular structure and order with second-harmonic generation microscopy", in *Second-Harmonic Generation Imaging*, F. S. Pavone and P. J. Campagnola, Eds., 2013, CRC Press, Chap. 4 (2013).

81. O. Nadiarnykh, S. Plotnikov, W. A. Mohler, I. Kalajzic, D. Redford-Badwal, P. J. Campagnola,

"Second harmonic generation imaging microscopy studies of osteogenesis imperfecta," *J. Biomed. Opt.* **12**, 051805 (2007).

82. R. LaComb, O. Nadiarnykh, P. J. Campagnola, "Quantitative second harmonic generation imaging of the diseased state osteogenesis imperfecta: Experiment and simulation," *Biophys. J.* **94**, 4504–4514 (2008).

83. K. M. Reiser, C. Bratton, D. R. Yankelevich, A. Knoesen, I. Rocha-Mendoza, J. Lotz, "Quantitative analysis of structural disorder in intervertebral disks using second harmonic generation imaging: Comparison with morphometric analysis," *J. Biomed. Opt.* **12**, 064019 (2007).

84. N. Tiwari, S. Chabra, S. Mehdi, P. Sweet, T. B. Krasieva, R. Pool, B. Andrews, G. M. Peavy, "Imaging of normal and pathologic joint synovium using nonlinear optical microscopy as a potential diagnostic tool," *J. Biomed. Opt.* **15**(056001), 056001 (2010).

85. S. J. Lin, R. J. Wu, H. Y. Tan, W. Lo, W. C. Lin, T. H. Young, C. J. Hsu, J. S. Chen, S. H. Jee, C. Y. Dong, "Evaluating cutaneous photoaging by use of multiphoton fluorescence and second-harmonic generation microscopy," *Opt. Lett.* **30**, 2275–2277 (2005).

86. M. J. Koehler, S. Hahn, A. Preller, P. Elsner, M. Ziemer, A. Bauer, K. König, R. Bückle, J. W. Fluhr, M. Kaatz, "Morphological skin ageing criteria by multiphoton laser scanning tomography: Non-invasive in-vivo scoring of the dermal fibre network," *Exp. Dermatol.* **17**, 519–523 (2008).

87. M. J. Koehler, A. Preller, N. Kindler, P. Elsner, K. Konig, R. Buckle, M. Kaatz, "Intrinsic, solar and sunbed-induced skin aging measured in vivo by multiphoton laser tomography and biophysical methods," *Skin Res. Tech.* **15**, 357–363 (2009).

88. J. Paoli, M. Smedh, A.-M. Wennberg, M. B. Ericson, "Multiphoton laser scanning microscopy on non-melanoma skin cancer: Morphologic features for future non-invasive diagnostics," *J. Invest. Dermatol.* **128**, 1248–1255 (2008).

89. C. Krafft, B. Dietzek, J. Popp, "Raman and CARS microspectroscopy of cells and tissues," *Analyst* **134**(6), 1046–1057 (2009).

90. M. Muller, A. Zumbusch, "Coherent anti-stokes Raman scattering microscopy," *Chemphyschem* **8**(15), 2156–2170 (2007).

91. J. X. Cheng, Y. K. Jia, G. F. Zheng, X. S. Xie, "Laser-scanning coherent anti-stokes Raman scattering microscopy and applications to cell biology," *Biophys.J.* **83**(1), 502–509 (2002).

92. A. X. Cheng, G. F. Zheng, S. N. Xie, "Real-time vibrational imaging of apoptosis with laser-scanning coherent anti-Stokes Raman scattering microscopy," *Biophys. J.* **82**(1), 175a–175a (2002).

93. C. L. Evans, E. O. Potma, M. Puoris'haag, D. Cote, C. P. Lin, X. S. Xie, "Chemical imaging of tissue in vivo with video-rate coherent anti-Stokes Raman scattering microscopy," *Proc. Natl. Acad. Sci. USA* **102**(46), 16807–16812 (2005).

94. H. W. Wang, T. T. Le, J. X. Cheng, "Label-free imaging of arterial cells and extracellular matrix using a multimodal CARS microscope," *Opt. Commun.* **281**, 1813–1822 (2008).

95. X. L. Nan, J. X. Cheng, X. S. Xie, "Vibrational imaging of lipid droplets in live fibroblast cells with coherent anti-Stokes Raman scattering microscopy," *J. Lipid Res.* **44**, 2202–2208 (2003).

96. E. O. Potma, X. S. Xie, "Detection of single lipid bilayers with coherent anti-Stokes Raman scattering (CARS) microscopy," *J. Raman Spectrosc.* **34**, 642–650 (2003).

97. N. Vogler, A. Medyukhina, I. Latka, S. Kemper, M. Boehm, B. Dietzek, J. Popp, "Towards multimodal nonlinear optical tomography — experimental methodology," *Laser Phys. Lett.* **8**, 617–624 (2011).

98. T. Meyer, N. Bergner, C. Bielecki, C. Krafft, D. Akimov, B. F. M. Romeike, R. Reichart, R. Kalff, B. Dietzek, J. Popp, "Nonlinear microscopy, infrared, Raman microspectroscopy for brain tumor analysis," *J. Biomed. Opt.* **16**, 021113 (2011).

99. C. L. Evans, X. Xu, S. Kesari, X. S. Xie, S. T. C. Wong, G. S. Young, "Chemically-selective imaging of brain structures with CARS microscopy," *Opt. Express.* **15**, 12076–12087 (2007).

100. C. L. Evans, E. O. Potma, M. Puoris'haag, D. Coté, C. P. Lin, X. S. Xie, "Chemical imaging of tissue in vivo with video-rate coherent anti-Stokes Raman scattering microscopy," *Proc. Natl. Acad. Sci. USA* **102**, 16807–16812 (2005).

101. S. Bégin, E. Bélanger, S. Laffray, R. Vallée, D. Coté, "In vivo optical monitoring of tissue pathologies and diseases with vibrational contrast," *J. Biophoton.* **2**, 632–642 (2009).

102. C. Krafft, A. A. Ramoji, C. Bielecki, N. Vogler, T. Meyer, D. Akimov, P. Roesch, M. Schmitt, B. Dietzek, I. Petersen, A. Stallmach, J. Popp, "A comparative Raman and CARS imaging study of colon tissue," *J. Biophoton.* **2**, 303–312 (2009).

103. B. C. Chen, J. Sung, S. H. Lim, "Chemical imaging with frequency modulation coherent anti-Stokes Raman scattering microscopy at the vibrational fingerprint region," *J. Phys. Chem. B* **114**, 16871–16880 (2010).

104. L. H. Laiho, S. Pelet, T. M. Hancewicz, P. D. Kaplan, P. T. So, "Two-photon 3-D mapping of

ex vivo human skin endogenous fluorescence species based on fluorescence emission spectra," *J Biomed Opt.* **10**(2), 024016 (2005).

105. K. Moezardalan, J. W. Birk, M. Tadros, F. A. Forouhar, O. Nadiarnykh, J. C. Anderson, P. J. Campagnola, "Second harmonic generation (SHG) laser: Useful in the diagnosis of malignant colonic-polyps," *Gastrointest. Endosc.* **71**, AB207 (2010).

106. S. Zhuo, X. Zhu, G. Wu, J. Chen, S. Xie, "Quantitative biomarkers of colonic dysplasia based on intrinsic second-harmonic generation signal," *J. Biomed. Opt.* **16**(12), 120501 (2011).

107. R. Cicchi, A. Sturiale, G. Nesi, D. Kapsokalyvas, G. Alemanno, F. Tonelli, F. S. Pavone, "Multiphoton morpho-functional imaging of healthy colon mucosa, adenomatous polyp and adenocarcinoma," *Biomed. Opt. Express.* **4**, 1204–1213 (2013).

108. R. Cicchi, A. Crisci, A. Cosci, G. Nesi, D. Kapsokalyvas, S. Giancane, M. Carini, F. S. Pavone, "Time- and spectral-resolved two-photon imaging of healthy bladder mucosa and carcinoma in situ," *Opt. Express* **18**(4), 3840–3849 (2010).

109. R. Cicchi, D. Massi, S. Sestini, P. Carli, V. De Giorgi, T. Lotti, F. S. Pavone, "Multidimensional non-linear laser imaging of basal cell carcinoma," *Opt Express* **15**(16), 10135–10148 (2007).

110. R. Cicchi, F. S. Pavone, "Non-linear fluorescence lifetime imaging of biological tissues," *Anal. Bioanal. Chem* **400**(9), 2687–2697 (2011).

111. J. L. Suhalim, C. Y. Chung, M. B. Lilledahl, R. S. Lim, M. Levi, B. J. Tromberg, E. O. Potma, "Characterization of cholesterol crystals in atherosclerotic plaques using stimulated raman scattering and second-harmonic generation microscopy," *Biophys. J.* **102**(8), 1988–1995 (2012).

112. R. M. Williams, W. R. Zipfel, W. W. Webb, "Interpreting second-harmonic generation images of collagen I fibrils," *Biophys. J.* **88**, 1377–1386 (2005).

113. J. Mertz, L. Moreaux, "Second-harmonic generation by focused excitation of inhomogeneously distributed scatterers," *Opt. Commun.* **196**, 325–330 (2001).

114. R. Cicchi, C. Matthaus, T. Meyer, A. Lattermann, B. Dietzek, B. R. Brehm, J. Popp, F. S. Pavone, "Characterization of collagen and cholesterol deposition in atherosclerotic arterial tissue using nonlinear microscopy," *J Biophoton.* **6**, doi 10.1002/jbio.201300055 (2013).

115. A. Walter, S. Erdmann, T. Bocklitz, E. M. Jung, N. Vogler, D. Akimov, B. Dietzek, P. Rosch, E. Kothe, J. Popp, "Analysis of the cytochrome distribution via linear and nonlinear Raman spectroscopy," *Analyst* **135**(5), 908–917 (2010).

116. D. Akimov, S. Chatzipapadopoulos, T. Meyer, N. Tarcea, B. Dietzek, M. Schmitt, J. Popp, "Different contrast information obtained from CARS and nonresonant FWM images," *J. Raman Spectrosc.* **40**(8), 941–947 (2009).

117. M. J. Buehler, S. Uzel, "Deformation and failure of collagenous tissues: A multi-scale study," *Proc. Asme Summer Bioengineering Conf. Parts A and B*, pp. 301–302 (2009).

118. N. Vogler, T. Meyer, D. Akimov, I. Latka, C. Krafft, N. Bendsoe, K. Svanberg, B. Dietzek, J. Popp, "Multimodal imaging to study the morphochemistry of basal cell carcinoma," *J. Biophotonics* **3**(10-11), 728–736 (2010).

119. J. Hagmar, C. Brackmann, T. Gustavsson, A. Enejder, "Image analysis in nonlinear microscopy," *J. Opt. Soc. Am. A-Optics Image Sci. Vis.* **25**(9), 2195–2206 (2008).

120. K. Konig, I. Riemann, "High-resolution multiphoton tomography of human skin with subcellular spatial resolution and picosecond time resolution," *J. Biomed. Opt.* **8**(3), 432–439 (2003).

121. F. Koenig, J. Knittel, L. Schnieder, M. George, M. Lein, D. Schnorr, "Confocal laser scanning microscopy of urinary bladder after intravesical instillation of a fluorescent dye," *Urology* **62**(1), 158–161 (2003).

122. G. A. Sonn, S. N. Jones, T. V. Tarin, C. B. Du, K. E. Mach, K. C. Jensen, J. C. Liao, "Optical biopsy of human bladder neoplasia with in vivo confocal laser endomicroscopy," *J. Urol.* **182**(4), 1299–1305 (2009).

123. M. E. Llewellyn, R. P. Barretto, S. L. Delp, M. J. Schnitzer, "Minimally invasive high-speed imaging of sarcomere contractile dynamics in mice and humans," *Nature* **454**(7205), 784–788 (2008).

124. D. R. Rivera, D. Kobat, C. Xu, "Miniaturized fiber raster scanner for endoscopy," *Proc. SPIE*, **7895**, Optical Biopsy Ix (2011).

125. D. R. Rivera, C. M. Brown, D. G. Ouzounov, I. Pavlova, D. Kobat, W. W. Webb, C. Xu, "Compact and flexible raster scanning multiphoton endoscope capable of imaging unstained tissue," *Proc. Natl. Acad. Sci. USA* **108**(43), 17598–17603 (2011).

126. F. Fischer, B. Volkmer, S. Puschmann, R. Greinert, W. Breitbart, J. Kiefer, R. Wepf, "Risk estimation of skin damage due to ultrashort pulsed, focused near-infrared laser irradiation at 800 nm," *J Biomed. Opt.* **13**(4), 041320 (2008).

127. O. Nadiarnykh, G. Thomas, J. Van Voskuilen, H. J. Sterenborg, H. C. Gerritsena, "Carcinogenic damage to deoxyribonucleic acid is induced by near-infrared laser pulses in multiphoton microscopy via combination of two- and three-photon

absorption," *J. Biomed. Opt.* **17**(11), 116024 (2012).

128. G. Thomas, O. Nadiarnykh, J. van Voskuilen, C. L. Hoy, H. C. Gerritsen, H. J. Sterenborg, "Estimating the risk of squamous cell cancer induction in skin following nonlinear optical imaging," *J. Biophotonics* (2013), doi: 10.1002/jbio.201200207.

129. M. C. Skala, K. M. Riching, A. Gendron-Fitzpatrick, J. Eickhoff, K. W. Eliceiri, J. G. White, N. Ramanujam, "In vivo multiphoton microscopy of NADH and FAD redox states, fluorescence lifetimes, cellular morphology in precancerous epithelia," *Proc. Natl. Acad. Sci. USA* **104**(49), 19494–19499 (2007).

130. J. A. Palero, A. N. Bader, H. S. de Bruijn, A. der Ploeg van den Heuvel, H. J. Sterenborg, H. C. Gerritsen, "In vivo monitoring of protein-bound and free NADH during ischemia by nonlinear spectral imaging microscopy," *Biomed. Opt. Express* **2**(5), 1030–1039 (2011).

131. X. Han, E. Brown, "Measurement of the ratio of forward-propagating to back-propagating second harmonic signal using a single objective," *Opt. Express* **18**(10), 10538–10550 (2010).